The Thesis Committee for Yimeng Wang
Certifies that this is the approved version of the following Thesis:

Electron Mobility in Monolayer WS_2 Encapsulated in Hexagonal Boron-Nitride

APPROVED BY
SUPERVISING COMMITTEE:

Emanuel Tutuc, Supervisor

L. Frank Register

Electron Mobility in Monolayer WS_2 Encapsulated in Hexagonal Boron-Nitride

by

Yimeng Wang

Thesis

Presented to the Faculty of the Graduate School of

The University of Texas at Austin

in Partial Fulfillment

of the Requirements

for the Degree of

Master of Science in Engineering

The University of Texas at Austin

April 2021

Acknowledgements

First of all, I would like to express my sincere appreciation and gratitude to my advisor, Prof. Emanuel Tutuc, for his continuous support and invaluable suggestions, as well as constant trust in me which always propels me to become a better researcher. I also want to thank Prof. L. Frank Register, who kindly agreed to serve as a reader for this thesis.

I would like to thank Kyoung Kim, for his tremendous help – form fabrication techniques to data analysis; from instrument operations to sketching skills. His creativity in fabrication of state-of-the-art 2D devices has always been inspiring for me.

I would like to thank the members of my group, past and present – Babak Fallahazad, Stefano Larentis, Hema C. P. Movva, Feng Wen, Will Burg, and Wooyoung Yoon – a group of talented people who are always there for stimulating discussions and are omnipotent to solve any problem in the lab. Many works in this thesis could not have been done without their collective effort to keep the lab in an orderly fashion.

The theoretical simulations in Chapter 5 are performed by Thibault Sohier and Matthieu Verstraete in Université de Liege. I would like to thank them for their time and effort devoted in this project, and for their helpful discussions.

I would also like to acknowledge the MRC administrative and technical staff, James Hiltzfelder, Darren Robbins, Christine Wood, Joyce Kokes, Gerlinde Sehne, Jesse James, Bill Ostler, and Ricardo Garcia.

I must also thank my brilliant friends who always share their accomplishments and frustrations in their research and life with me and always listen to mine: Qiuying Lai, Tianyi Sun, Yajie Huang, Ye Peng, Xiao Wan, Junyi Liu, Ruijing Ge, Yaodan Hu, and Qiyuan Deng. I am grateful for the sisterhood which always makes me feel joyful, warm, and encouraged.

Finally, I thank my grandparents and parents, for their constant love, care, and support, and my boyfriend, Ao Cai, who always stands by me and truly respects me, for making me feel strong.

Abstract

Electron Mobility in Monolayer WS_2 Encapsulated in Hexagonal Boron-Nitride

Yimeng Wang, MSE

The University of Texas at Austin, 2021

Supervisor: Emanuel Tutuc

We report electron transport measurements in dual-gated monolayer WS_2 encapsulated in hexagonal boron-nitride. Using gated Ohmic contacts which operate from room temperature down to 1.5 K, we measure the intrinsic conductivity and carrier density as a function of temperature and gate bias. An intrinsic electron mobility of 100 $cm^2/(V \cdot s)$ at room temperature, and 2,000 $cm^2/(V \cdot s)$ at 1.5 K are achieved. The mobility shows a strong temperature dependence at high temperatures, consistent with phonon scattering dominated carrier transport. At low temperature, the mobility saturates due to impurity and long-range Coulomb scattering. First principles calculations of phonon scattering in monolayer WS_2 are in good agreement with the experimental results, showing we approach the intrinsic limit of transport in these 2D layers.

Table of Contents

List of Tables

List of Figures

Chapter 1: Introduction

Transition metal dichalcogenides (TMDs) are a family of materials in the form MX_2, where M stands for a transition metal (Mo, W, etc.) and X stands for a chalcogen (S, Se, or Te).[1,2] The TMDs are layered materials, each layer consisting of two sheets of X atoms and one of M atoms sandwiched in X atoms. Atoms in each layer are bonded covalently, Figure 1.1 shows the schematics of TMD in the X-M-X monolayer form.

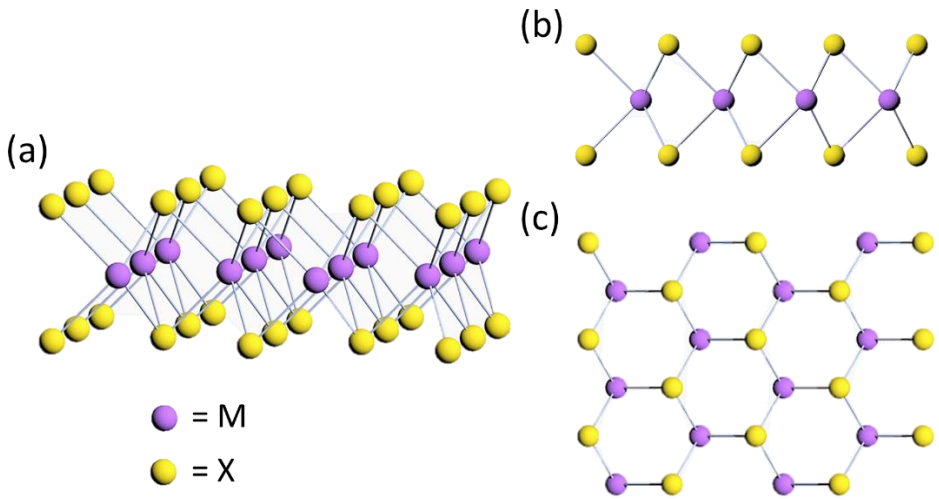

Figure 1.1: (a) Schematic of a TMD monolayer structure and when viewed along the (b) in-plane and (c) out-of-plane directions.

The TMDs in bulk form consist of X-M-X monolayers stacked together, with individual monolayers coupled by van der Waals forces.[3] Because van der Waals forces are weaker than the covalent bonds between the X and M atoms, TMD monolayers can be isolated by mechanical exfoliation, which will be introduced in details in Chapter 2.

Studies of TMDs in the monolayer form have become an emerging research area because of their significantly different properties compared with the bulk compound, due to quantum mechanical confinement effects.[4] The indirect to direct gap transition when reducing TMD thickness from a few-layers to the monolayer limit was first found in 2010,[5,6] followed by the discovery of intriguing electronic and photoelectronic properties leading to many applications, such as high-ON/OFF-ratio field-effect transistors (FETs),[7–11] phototransistors,[12] and ultrasensitive photodetectors.[13] Moreover, due to a lack of crystal inversion symmetry, the spin and valley degrees of freedom in TMD monolayers are coupled, providing great platform for exploring spin and valley physics. For example, experimental evidence of valley polarization was found in monolayer MoS_2,[14] as well as spin and valley Hall effects.[15,16]

	Lattice constant (Å)	m_K^c (meV)	m_Q^c (meV)	m_K^v (meV)	m_K^v (meV)
MoS_2	3.14	0.51	0.76	0.58	4.05
$MoSe_2$	3.27	0.64	0.80	0.71	7.76
WS_2	3.10	0.31	0.60	0.42	4.07
WSe_2	3.25	0.39	0.64	0.51	7.77

Table 1: Lattice constants and theoretically predicted effective masses at relevant valleys/peaks in some TMDs. Superscripts c and v denote the conduction and valence bands, respectively. Subscripts K and Q denote the K and Q valleys/peaks, respectively. Table adapted from TABLE I in Ref. [17].

Tungsten Disulfide (WS_2) is one member of the TMD family with an indirect bandgap of 1.3–1.4 eV in bulk form, and a direct bandgap of 2.3–2.4 eV in monolayer form.[18,19] WS_2 is interesting among other TMD materials for its predicted lightest effective

mass.[17,20,21] Table 1 lists lattice constants and theoretically predicted effective masses of some TMD materials, with data adapted from TABLE I in Ref. [17]. The WS_2 electron effective mass in both K and Q valleys are the lightest among the listed four TMD materials, leading to potentially high carrier mobility and strong spin-orbit interaction.

		Ref. [22]	Ref. [23]	Ref. [24]	Ref. [25]	Ref. [26]
Device structure		Ionic liquid-gated	WS_2 on SiO_2	WS_2 on SiO_2	h-BN-encapsulated	WS_2 on Al_2O_3
Layer thickness		Few-layer	Monolayer	Few-layer	Monolayer	Monolayer
Evaluation method		Hall	4-pt FE	2-pt FE	2-pt FE	4-pt FE
Mobility ($cm^2/(V \cdot s)$)	RT	65	40	234	214	83
	LT	-	140 (7 K)	250 (4 K)	486 (5 K)	337 (25 K)

Table 2: Previous published studies on electron transport properties of thin layer WS_2. The device structure, layer thickness, and electron mobility evaluation methods are listed, as well as room temperature (RT) and low temperature (LT) mobilities measured.

The electrical and optical properties of few-layer WS_2 have been reported in various studies. For example, high-mobility field-effect transistors based on few-layer WS_2 have been demonstrated down to monolayer thickness, with the electron mobilities reported as high as ~200 $cm^2/(V \cdot s)$ at room temperature and ~500 $cm^2/(V \cdot s)$ at low temperatures.[25,26] Photoluminescence studies have been performed on few-layer WS_2 as well, and the evidence of strong spin-valley coupling was found.[27–29] The focus of this thesis will be on the intrinsic electron transport in WS_2 in the monolayer limit. To show the novelty of this

work, we compare previous electronic transport studies on WS_2 thin layers and the electron mobilities measured therein (Table 2). In Table 2, mobility evaluation methods are listed as two-point field-effect (2-pt FE), four-point field-effect (4-pt FE), or Hall. These evaluation methods will be introduced and discussed in Chapter 4. The Hall mobility is the most accurate estimation of the true electron mobility and is used to assess intrinsic mobility. By investigating the Hall mobility (intrinsic mobility) in dual-gated FETs based on monolayer WS_2 encapsulated in hexagonal boron-nitride (h-BN) at cryogenic temperature down to 1.5 K and comparing the intrinsic mobility with the two- and four-point mobilities, we found that, generally, the two-point field-effect method underestimates and the four-point overestimates the electron mobility. A high electron mobility of ~2,000 $cm^2/(V \cdot s)$ is achieved in our samples, three times higher than the previously reported highest electron mobility.[25]

Chapter 2: Preparation and Characterization of Monolayer WS_2 [1]

2.1 MICROMECHANICAL EXFOLIATION

The monolayer WS_2 flakes used to fabricate WS_2 FETs are produced by micromechanical exfoliation, sourced from WS_2 crystals available commercially. Two different micromechanical exfoliation methods are used – regular micromechanical exfoliation, and gold-assisted micromechanical exfoliation.

2.1.1 Regular Micromechanical Exfoliation

The widely used micromechanical exfoliation method (the "Scotch tape" method) was firstly developed to isolate monolayer graphene.[30] The method was then applied to other layered materials including TMDs and hexagonal Boron Nitride. Evolved from the original method reported in Ref. [30], the current method is completely dry, with no solvent involved, which helps to maintain the pristine quality of the flakes.

The tape used for exfoliation in this study is commercially available at UltraTape. Starting from a small piece of WS_2 crystal (commercially available at HQ Graphene) transferred on the tape, the crystal is delaminated into thinner layers by repeatedly duplicating the crystal on the tape. The tape is then placed face-down on a polydimethylsiloxane (PDMS) film and peeled off to transfer the WS_2 mesas onto the PDMS. A SiO_2/Si chip is subsequently placed on the PDMS with the polished side in contact with the PDMS and removed rapidly from the PDMS to transfer the thin WS_2 flakes on the SiO_2/Si substrate. The SiO_2/Si substrate is cleaved from highly doped n-type silicon

[1] Part of this chapter and the following chapters have been published as Y. Wang, T. Sohier, K. Watanabe, T. Taniguchi, M. J. Verstraete, and E. Tutuc , "Electron mobility in monolayer WS_2 encapsulated in hexagonal boron-nitride", Applied Physics Letters 118, 102105 (2021). The author of this thesis, Y. Wang, fabricated and characterized the WS_2 samples, and contributed to the data analysis and the writing of the paper.

wafers with 285 nm thick thermally-grown SiO_2. Using PDMS to transfer WS_2 on SiO_2/Si helps to improve the yield of few-layer flakes in practice.

2.1.2 Gold-Assisted Micromechanical Exfoliation

Gold is known to have strong affinity to chalcogens, especially for sulfur atoms, with a strong S-Au bond strength estimated to be ~ 45 kcal/mole.[31,32] Because the interactions between the gold and the TMD at their interface is stronger than the interlayer van der Waals interactions in the TMD bulk, using gold to isolate large area monolayer TMDs is possible. To exploit this, gold-assisted exfoliation for TMD materials was proposed.[33,34]

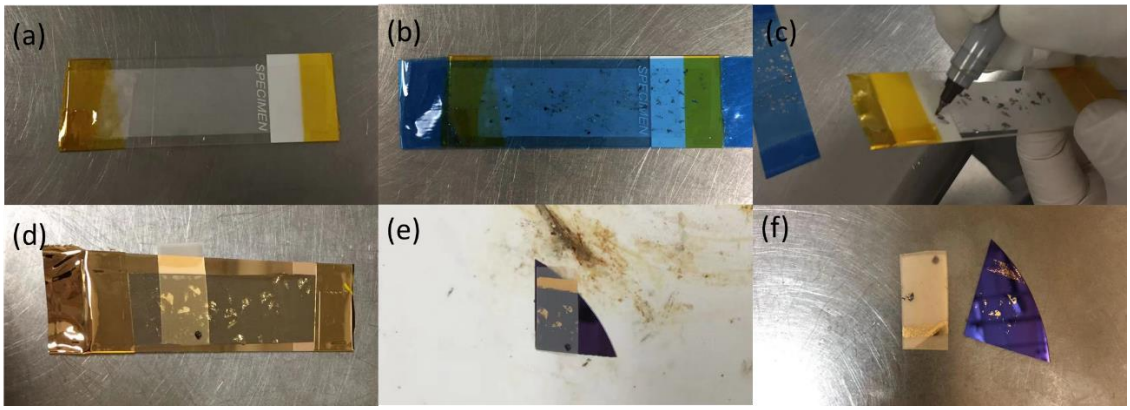

Figure 2.1: Process flow of gold-assisted exfoliation. (a) A glass slide with double-sided tape attached. (b) Transfer WS_2 mesas from UltraTape to the double-sided tape. (c) UltraTape is peeled off, leaving WS_2 mesas on the double-sided tape. Sample information is labeled on the glass slide. (d) ~40 nm thick gold is deposited. A piece of thermal release tape is used to transfer the gold layer and the topmost WS_2 layers onto a SiO_2/Si substrate. (e) A SiO_2/Si substrate is baked with the thermal release tape at 90 °C to release the gold layer and the topmost WS_2 layers. (f) The thermal release tape and the SiO_2/Si substrate after bake.

Figure 2.1 shows the process flow of the gold-assisted exfoliation. On a glass slide, a double-sided tape is attached [Fig 2.1 (a)]. A tape with WS_2 thin mesas prepared by similar steps to those described in Section 2.1.1 is placed face-down on the double-sided tape [Fig. 2.1 (b)] and then peeled off to leave thin WS_2 mesas on the double-sided tape [Fig. 2.1 (c)]. Gold (~40 nm thickness) is subsequently thermally deposited on the WS_2. Figure 2.1 (d) shows a piece of thermal release tape on the glass slide after gold deposition. The thermal release tape is peeled off with gold and the topmost layers of WS_2 and placed on a SiO_2/Si substrate. The substrate and the thermal release tape are then baked at 90 °C [Fig. 2.1 (e)] to release the gold and thin WS_2 flakes onto the substate [Fig. 2.1 (f)].

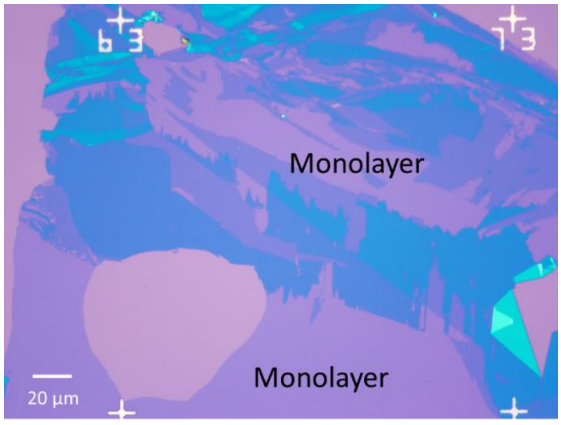

Figure 2.2: A large monolayer WS_2 flake obtained by gold-assisted exfoliation. The spacing between the adjacent alignment marks is 200 µm.

After the process above, some few-layer WS_2 flakes are released on the SiO_2/Si substrate, as well as a layer of gold on top. To remove the gold layer, the SiO_2/Si substrate is etched in potassium iodide and iodine (KI/I_2) wet etch for ~40 s. Figure 2.2 shows a large monolayer flake obtained by gold-assisted exfoliation. The size of the monolayer flakes exfoliated by this method ranges from 20×20 μm^2 to 200×200 μm^2. The exfoliated WS_2

flakes are characterized by atomic force microscopy (AFM) and photoluminescence (PL), as well as electrical transport at low temperature. The results show that the gold-assisted exfoliated WS_2 flakes are of similar quality to the regular exfoliated ones.

2.2 MONOLAYER CHARACTERIZATION

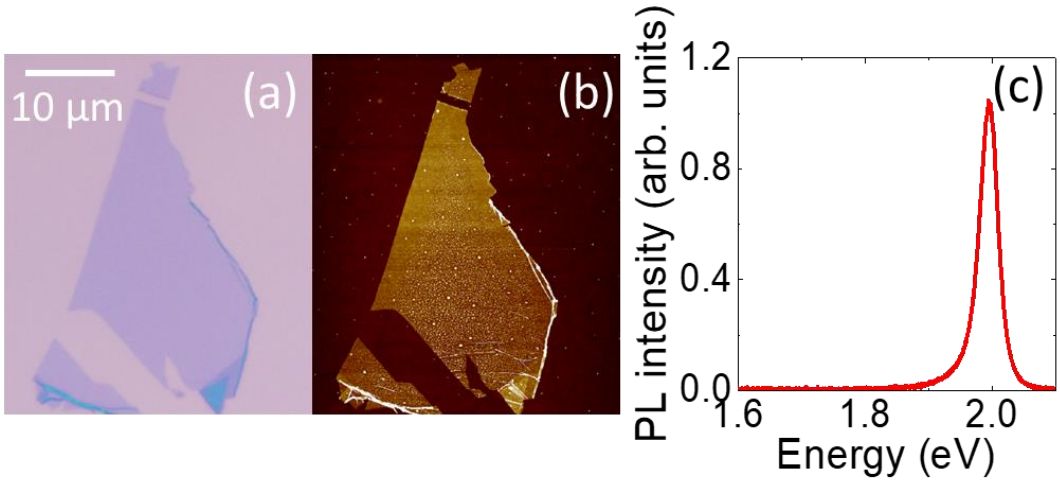

Figure 2.3: Optical micrography, AFM image, and Photoluminescence spectra acquired on a monolayer WS_2 flake. (a) Optical micrography of a WS_2 monolayer on SiO_2/Si substrate. (b) AFM topography of the same monolayer flake in (a). (c) Photoluminescence spectra acquired on the same flake shown in (a) and (b).

The exfoliated flakes are first identified by optical microscopy. Isolated and flat monolayer flakes of ~10×20 μm^2 size without adjacent few-layer stacking are chosen. The flakes are then characterized by AFM and PL. Figure 2.3 (a) shows an optical micrograph of a gold-assisted exfoliated monolayer WS_2 flake. The topography of the flake probed by AFM is shown in Fig. 2.3 (b). A PL measurement is then performed on the same flake [Fig. 2.3 (c)]. In contrast to the PL spectra of multi-layer WS_2, which have lower intensity and display multiple peaks associated with indirect gap transitions, the spectrum of the

monolayer WS_2 exhibits a single strong peak at 2.0 eV associated with direct gap emission, consistent with previous observations.[4,27,29] This further confirms the thickness of the monolayer WS2 flake.[27] The high intensity of PL spectrum also illustrates the high quality of the monolayer WS_2 flake.

Chapter 3: Device Fabrication and Structure

3.1 DRY TRANSFER TECHNIQUE

The advances of deterministic transfer techniques have been an impetus for the development of the 2D van der Waals heterostructure research field. From the first developed wet transfer[35] to the more versatile dry transfer techniques,[36] more and more complex 2D systems can be fabricated with much higher yield. All the devices investigated in this thesis are fabricated using dry transfer techniques, where a hemisphere PDMS stamp is used as a handle to selectively pick up and stack desired WS_2 or h-BN flakes. On the hemisphere PDMS handle, a thin layer of polypropylene carbonate (PPC) dissolved in anisole is spin-coated, and subsequentially baked at 180 °C to harden the PPC layer, which will serve as an adhesion layer to pick up thin flakes at raised temperature. The diameter of the hemisphere handle can range from one millimeter to a few millimeters. Smaller diameter limits the contact area between the polymer handle and the substrate, which will improve the selectivity of the pick-up, while larger diameter handles provide better control of the contact area radius in micrometer range.

Figure 3.1 demonstrates a typical workflow of a dry transfer process. Starting from a SiO_2/Si substrate with the desired flake (flake A) to be picked up [Fig. 3.1 (a)], the polymer hemisphere handle makes contact with the substrate at the location of flake A [Fig. 3.1 (b)] and picks it up at 40-50 °C [Fig. 3.1 (c)]. Another SiO_2/Si substrate with the target flake (flake B) to place flake A on is positioned under the polymer hemisphere handle with flake A on the handle [Fig. 3.1 (d)]. Another contact is then made with flake A and B aligned [Fig. 3.1 (e)]. Flake A is subsequently released on the substrate at a temperature > 90°C. The stack of flake A on B is then formed [Fig. 3.1 (f)]. By following the above steps repeatedly, any desired heterostructure stacks (usually within 5 layers) can be achieved.

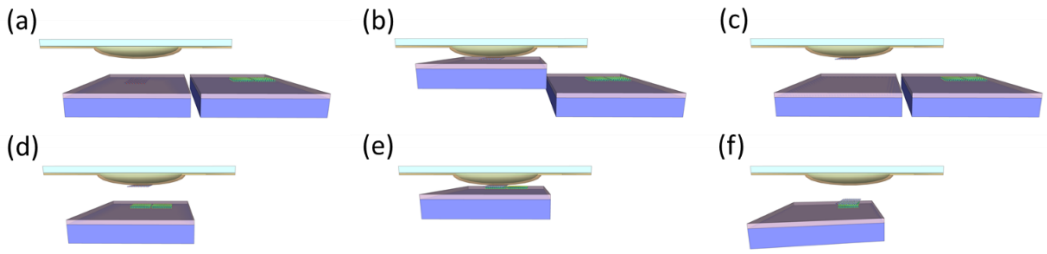

Figure 3.1: Illustration of a typical dry transfer process. (a) Polymer hemisphere handle above flake A on SiO_2/Si substrate. (b) Polymer hemisphere handle making contact to the substrate. (c) Flake A is picked up on the polymer hemisphere handle. (d) Substrate with flake B is placed under the polymer hemisphere handle. (e) Polymer hemisphere handle making contact to the substrate on flake B. (f) Flake A is released on flake B.

3.2 DEVICE PROCESS FLOW

The WS_2 devices investigated in this thesis consist of one WS_2 monolayer, two gate dielectrics (h-BN), metal back contacts, and two gates (top gate and back gate). Figure 3.2 shows the process flow with the optical micrographs taken during the fabrication process. Panel (a) is an optical image of a WS_2 monolayer produced by gold-assisted micromechanical exfoliation, described in Section 2.1.2, and characterized using the methods described in Section 2.2. Using the dry transfer technique described in Section 3.1, an h-BN flake of ~30 nm thickness is placed on the WS_2 monolayer [Fig. 3.2 (b)]. On another SiO_2/Si substrate, a rectangular Pt metal back gate of ~10 nm thick is patterned and covered by an h-BN flake of ~25 nm thickness [Fig. 3.2 (c)]. A set of metal back contacts is subsequently patterned with Cr/Pd or Cr/Pt (15~20 nm thick) [Fig. 3.2 (d)]. The stack in Fig. 3.2 (b) is then placed on the back contacts to form the stack in Fig. 3.2 (e). The device is completed by depositing the top gate and contact extensions with Cr/Pd/Au [Fig. 3.2 (f)].

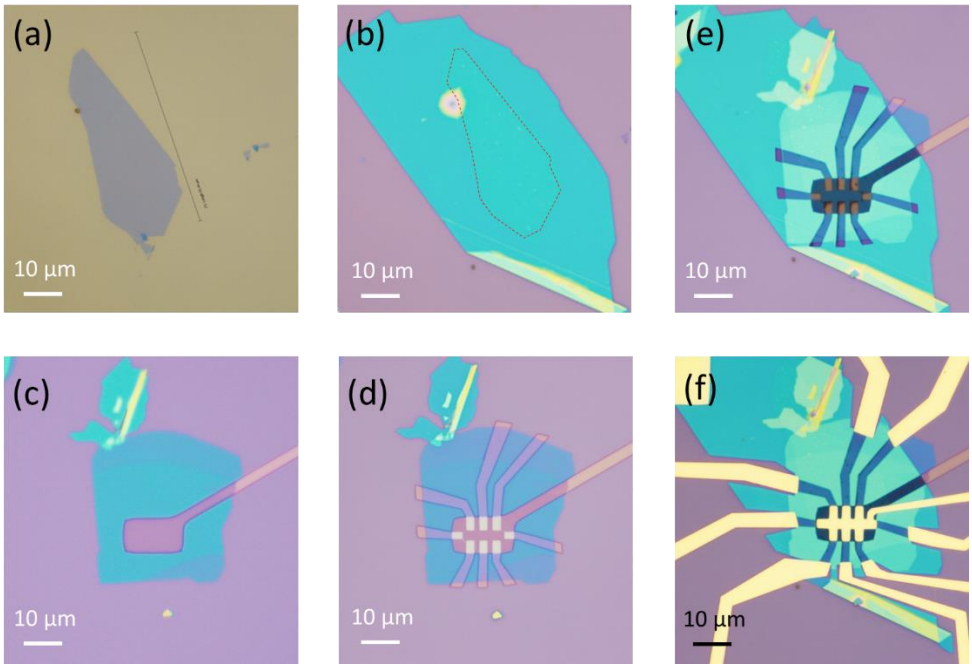

Figure 3.2: Process flow of the device fabrication demonstrated with false-color optical micrographs. (a) Monolayer WS_2 on SiO_2/Si substrate. (b) Top h-BN on the monolayer WS_2. (c) Metal back gate covered by h-BN. (d) Pt contacts patterned on h-BN/back gate. (e) Heterostructure stack in (b) placed on stack in (d). (f) The final device with metal top gate. The scale bars represent 10 µm.

3.3 DEVICE STRUCTURE

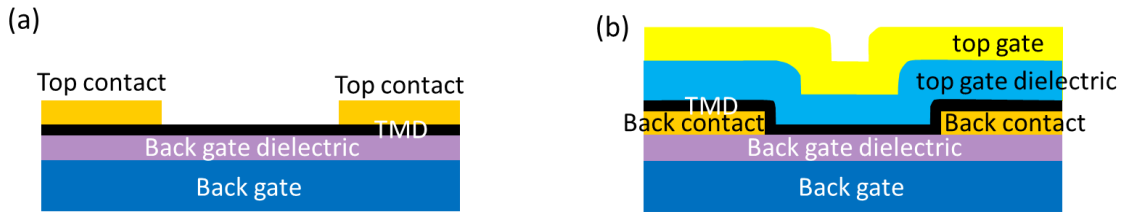

Figure 3.3: Top-contacted (a) and back-contacted (b) architecture of TMD FETs.

The back-contacted architecture [Fig. 3.3 (b)] is employed to improve the WS_2-to-metal contact. The back-contacted architecture in TMD devices is found to exhibit lower contact resistance compared to the top-contacted one. In the top-contacted architecture the metal contacts are directly deposited on the TMD layer [Fig. 3.3 (a)]. In top-contacted structures, an adhesion layer (Cr or Ni) is needed because Pt and Pd have poor adhesion to TMDs. Thus, the metal interface directly contacting the TMD is the adhesion layer metal which easily oxidizes and has a lower work function that leads to a higher Schottky barrier at the TMD-to-metal interface. Furthermore, the TMD-to-metal interface in the top-contacted structure can be largely affected by the deposition conditions, such as vacuum level in the deposition chamber, deposition rate, deposition temperature, etc. The back-contacted architecture, however, circumvents the above problems. First, the metal at the TMD-to-metal interface is an inert metal with a high work function. Second, the back contact deposition is decoupled from creating the TMD-to-metal interface, avoiding variations of the contact quality resulting from variations of the deposition conditions. In addition, the surface of the metal back contacts can be annealed to improve surface smoothness and be characterized by AFM before the TMD-to-metal contact is formed, making it possible to avoid using metals with rough surfaces inadvertently. Figure 3.4 shows AFM images of (a) a set of Pt metal contacts and (b) the device made with the same set of contacts. Although some high grains can be observed near the contact edges, most of the metal surface area is very clean and flat for the WS_2 to make good contact to. The resulting device also shows flat topology around the contact areas.

The monolayer WS_2 devices are structured as dual-gated FETs. As shown in Fig. 3.4 (b), the top gate is patterned into a Hall-bar shape and defines the active area of the device. The Hall-bar shaped channel provides various measuring configuration options

such as two-point, four-point, and Hall effect measurements. The top gate serves as a primary gate for FET operation, and local back gate is used to tune the FET characteristics. The local back gates also have the advantage over to Si back-gated devices of enabling individual gate control when having multiple FETs on the same substrate. Two dual-gated and h-BN encapsulated WS_2 monolayers are investigated in this study, labelled device A and B.

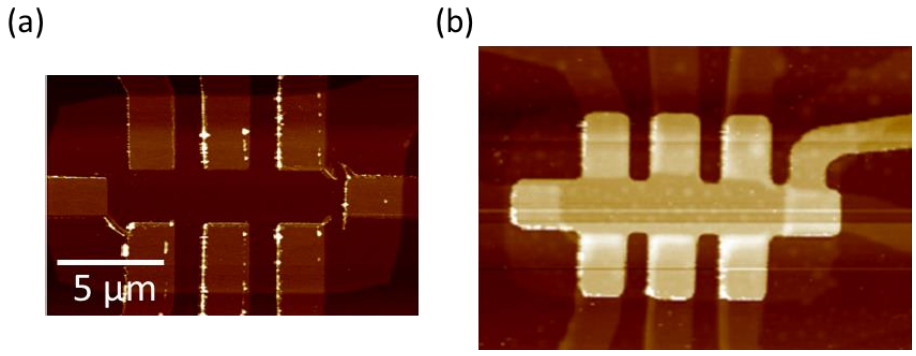

Figure 3.4: AFM images of (a) a set of Pt contacts before WS_2 is transferred on, and (b) the WS_2 device made with the contacts in (a).

Chapter 4: Electrical Transport

4.1 Output Characteristics and Transfer Characteristics

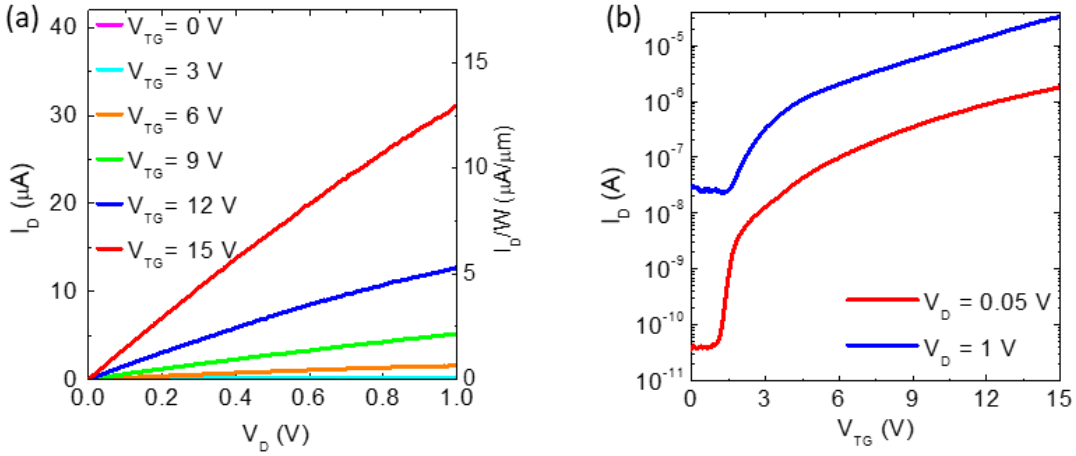

Figure 4.1: Room temperature characteristics. (a) I_D vs. V_D at various top gate biases. The linear dependence of I_D-V_D is evidence of Ohmic contacts. (b) I_D vs. V_{TG} at drain biases V_D = 0.05 V and 1 V. The ON/OFF ratio is around 10^5 at V_D = 0.05 V. Data is taken in vacuum at room temperature for all measurements in this figure.

The characteristics of the monolayer WS_2 devices are first investigated at room temperature. Figure 4.1 (a) shows the room temperature output characteristics, namely drain current (I_D) vs. drain voltage (V_D) measured at different top-gate voltages (V_{TG}), and at a back-gate bias $V_{BG} = 0$ V for device A. The linear I_D-V_D response at low drain bias confirms the metal-to-WS_2 contacts are ohmic. However, as we show in this study, the metal-to-WS_2 contact resistance has a strong dependence on V_{TG}. Figure 4.1 (b) shows the transfer characteristics, I_D vs. V_{TG}, measured at drain biases of V_D = 0.05 V and V_D = 1 V. Unlike a conventional FET, the I_D shows a strong, almost exponential dependence on V_{TG} even above the threshold voltage, indicated at V_D = 0.05 V by a slope change at

$V_{TG} \cong 2$ V. The strong I_D vs. V_{TG} dependence, both below and above threshold is common to Schottky barrier FET characteristics, and explained by a gate-voltage-dependent contact resistance. The top gate leakage current is lower than 1 nA in all measurements.

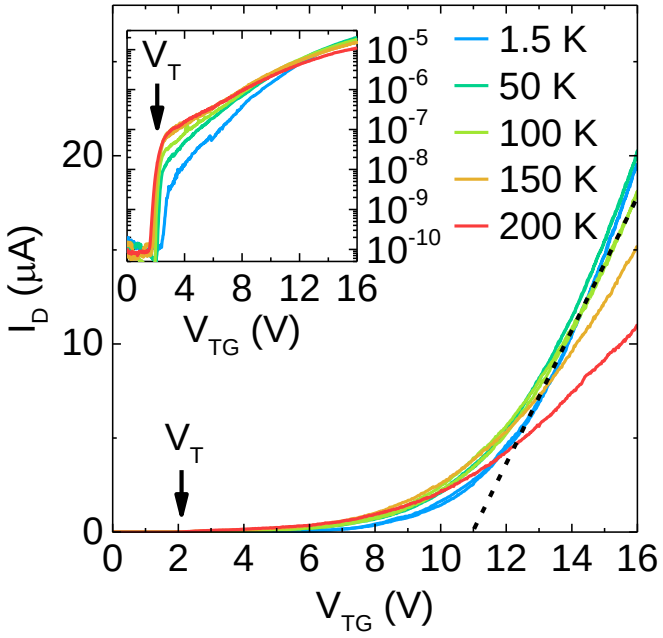

Figure 4.2: Temperature dependence of I_D vs. V_{TG} on a linear scale and (inset) log-linear scale, measured at $V_D = 0.5$ V. The arrows mark the V_T extracted from the Hall density measurements. A linear extrapolation of the I_D vs. V_{TG} data (dashed line) at 100 K intercepts the V_{TG} axis at a value significantly larger than V_T.

The transfer characteristics are then investigated at a temperature range 1.5 – 200 K. In Fig. 4.2 we show the temperature dependence of transfer characteristics, I_D vs. V_{TG} measured at $V_D = 0.5$ V. The main panel in Fig. 4.2 shows that a linear extrapolation at 100 K of the I_D vs. V_{TG} intercepts the *x*-axis at $V_{TG} \cong 11$ V, a value significantly larger than the threshold voltage $V_T = 2.1$ V at which the Hall density $n = 0$. This behavior

illustrates the differences between the WS_2 FET characteristics, and conventional FETs with highly doped source and drain. Therefore, applying a conventional FET analysis will largely overestimate the threshold voltage, and underestimate the carrier density at a given V_{TG} value. In Fig. 4.2 inset, we show the same dataset on log-linear scale, along with the V_T determined from Hall measurements. Similar to Fig. 4.1 (b) data, I_D has an exponential dependence on V_{TG}, with a marked change in slope at $V_{TG} \approx V_T$. This dataset suggests that a better V_T estimation can be obtained from the V_{TG} value at which the exponential I_D vs. V_{TG} dependence changes slope. Lastly, we note that the V_T is weakly dependent on temperature. The variation of the threshold voltage over the range of temperature in our study is ~0.5 V, corresponding to a carrier density variation of 3×10^{11} cm^{-2}.

4.2 HALL EFFECT

4.2.1 Classical Hall Effect in 2D Electron Systems

The Hall effect was discovered by Edwin Hall in 1879.[37] An illustration of the Hall effect setup is shown in Fig. 4.3, where the electrons are restricted to move in the x-y plane. A constant magnetic field $\boldsymbol{B}$ is applied in the z-direction while a current I_x flows in the x-direction.

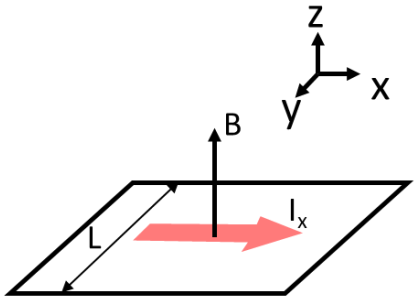

Figure 4.3: Illustration of the classical Hall effect.

Solving Ohm's law $\boldsymbol{J} = \sigma \boldsymbol{E}$, where $\boldsymbol{J}$ is the current density and $\boldsymbol{E}$ is the electric field in x-direction, one gets

$$\sigma = \begin{pmatrix} \sigma_{xx} & \sigma_{xy} \\ -\sigma_{xy} & \sigma_{xx} \end{pmatrix} = \begin{pmatrix} 1 & \omega_B \tau \\ -\omega_B \tau & 1 \end{pmatrix}, \tag{4.1}$$

where $\omega_B = eB/m$ is the cyclotron frequency, and τ is the momentum relaxation time. σ is called the conductivity tensor,

The resistivity is defined as the inverse of the conductivity

$$\rho = \sigma^{-1} = \begin{pmatrix} \rho_{xx} & \rho_{xy} \\ -\rho_{xy} & \rho_{yy} \end{pmatrix} = \frac{m}{ne^2\tau} \begin{pmatrix} 1 & -\omega_B \tau \\ \omega_B \tau & 1 \end{pmatrix}. \tag{4.2}$$

For a sample with a length L in the y-direction, a voltage V_y will be dropped in y-direction, and the transverse resistance can be measured by dividing the voltage V_y with the x-direction current I_x

$$R_{xy} = \frac{V_y}{I_x} = \frac{LE_y}{LJ_x} = \frac{E_y}{J_x} = -\rho_{xy}, \tag{4.3}$$

R_{xy} is defined as the Hall resistance,

$$R_{xy} = \frac{m}{ne^2\tau} \times \omega_B \tau = \frac{B}{ne}. \tag{4.4}$$

It is worth noting that at low temperature and under a strong magnetic field, classical Hall effect will not be valid anymore, and quantum Hall effect will take over.[38–40] However, in this thesis, we will probe Hall resistance at T = 100 K and in moderate magnetic fields, where the linear relationship between R_{xy} and B still holds, that is, the experimental observation can be explained by classical Hall effect. Because the quantum Hall effect is not relevant to this study, it will not be discussed in this thesis.

4.2.2 Hall Measurements and Density Extraction

The Hall resistances are measured in perpendicular magnetic fields (B) up to 7 T, at a temperature T = 100 K. Figure 4.4 (a) and (b) show the Hall resistance (R_{xy}) vs. B at

different V_{TG} [panel (a)] and V_{BG} [panel (b)] values. The slope of R_{xy} vs. B data allows the extraction of the electron density (n) using Eq. (4.4). Figure 4.4 (a) and 4.4 (b) insets shows the extracted n vs. V_{TG} and n vs. V_{BG}, respectively. The linear fits to n vs. V_{TG} and n vs. V_{BG} yield the gate capacitances C_{TG} and C_{BG}, respectively. The carrier density can then be extracted at different gate biases via the relation $en = C_{TG}V_{TG} + C_{BG}V_{BG} + en_0$. The top gate capacitance of device A is C_{TG} = 103 nF/cm^2, back gate capacitance C_{BG} = 163 nF/cm^2, and n_0 = -1.34×10^{12} cm^{-2}. We assume that the same carrier density-gate bias relation holds for all temperatures for the following discussion.

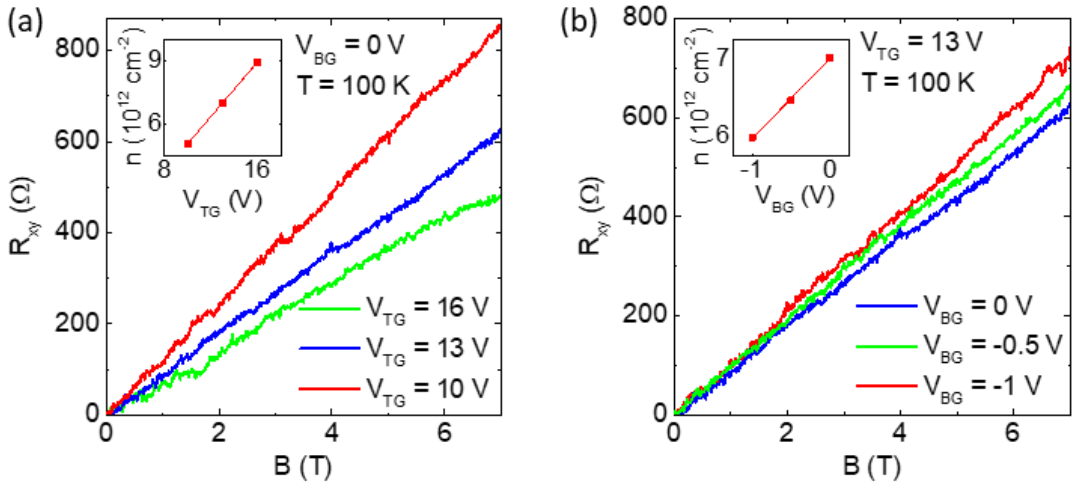

Figure 4.4: Hall density extraction. (a) R_{xy} vs. B measured for different V_{TG} values, at $V_{BG} = 0$ V and T = 100 K. (b) R_{xy} vs. B measured for different V_{BG} values, at $V_{TG} = 13$ V and T = 100 K. R_{xy} is linearly dependent on B. Linear fits to R_{xy} vs. B data yield the carrier densities. Insets: (a) n vs. V_{TG} and (b) n vs. V_{BG}; symbols represent the extracted values, and lines are the linear fits.

4.3 CONDUCTIVITY AND CONTACT RESISTANCE

Using the outer contacts as source and drain for current injection, and the inner contacts as voltage probes (ΔV), the four-point channel conductance $G_{4pt} = I_D/\Delta V$ can be measured, as well as the intrinsic channel conductivity $G_\square = G_{4pt} \times L/W$, where W = 2.4 μm is the width of the channel, and L = 3.5 μm is the distance between the centers of the neighboring contacts.

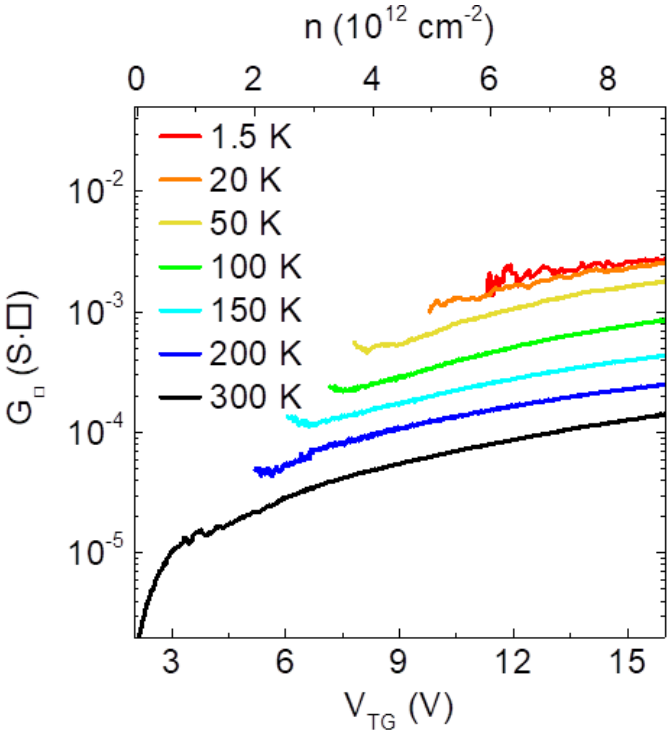

Figure 4.5: $G_\square$ vs. V_{TG} and n (top axis) measured at various temperatures. The conductivity increases monotonically with decreasing temperature, suggesting a metallic phase.

Figure 4.5 shows $G_\square$ vs. V_{TG} and n at various temperatures ranging from 1.5 K to 300 K. We note that at reduced temperatures the contact resistance increases at a fixed electron density, which in turn affects the accuracy of the four-point measurement. This is

reflected in $G_{\square}$ vs. n data of Fig. 4.5, where the accessible electron density range is gradually reduced with decreasing temperature. A linear dependence of $G_{\square}$ vs. V_{TG} is observed at all temperatures. Furthermore, $G_{\square}$ increases monotonically with reducing T, indicating a metallic phase of 2D electrons in WS_2.

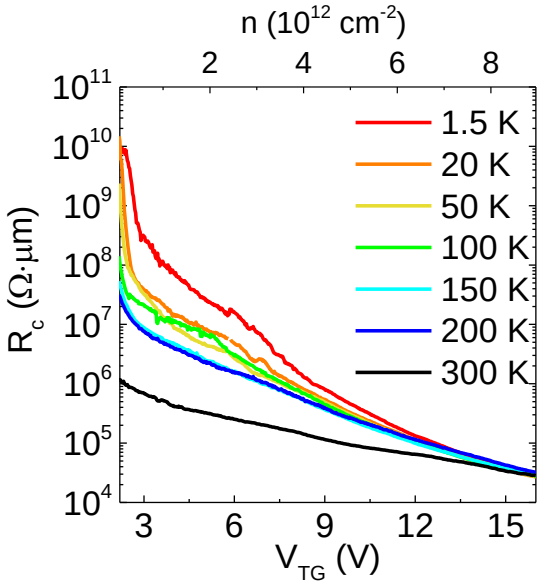

Figure 4.6: R_c vs. V_{TG} and n (top axis) at different temperatures. The contact resistance shows a strong dependence on V_{TG}, particularly at reduced temperatures. At high V_{TG} the R_c values depend weakly on temperatures, consistent with tunneling through the Schottky barrier at the metal-WS_2 contact.

The four-point conductance G_{4pt} probes the intrinsic channel conductance compared to the two-point conductance $G_{2pt} = I_D/V_D$, because the former excludes contact resistances of the source and drain terminals. By subtracting the four-point resistance $1/G_{4pt}$ from the two-point resistance $1/G_{2pt}$, we can estimate the specific contact resistance $R_C = (1/G_{2pt} - 1/G_{4pt}) \times W_C/2$, where W_C represents the contact width of source/drain terminal. The R_C vs. V_{TG} and n measured at various T values are shown in Fig. 4.6. At low electron densities, the contact resistance has a strong temperature

dependence, and increases with decreasing temperature. This observation can be explained by a diminished thermally-activated injection over the metal-to-WS_2 Schottky barrier. However, at high electron densities, the contact resistance becomes less sensitive to temperature, and remains relatively low down to 1.5 K. The insensitivity to temperature suggests the electron injection is controlled by tunneling through the Schottky barrier at the metal-to-WS_2 contact, which in turn is achieved by inducing a large electron density in the channel around the metal-to-WS_2 interface, resulting in a tunnel barrier with reduced thickness.[41,42]

4.4 MOBILITY EXTRACTION

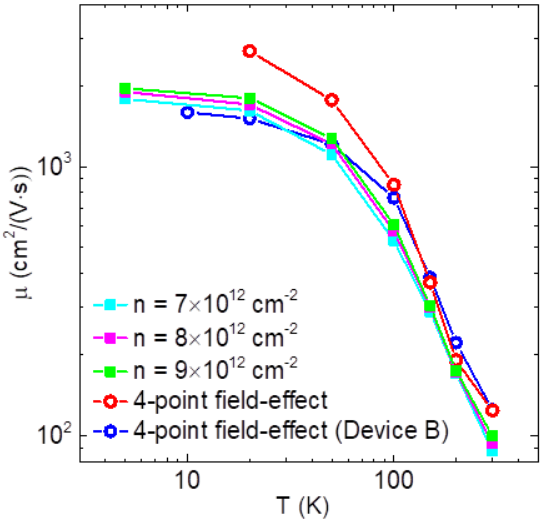

Figure 4.7: Temperature dependence of the intrinsic and field-effect mobility. Unless noted, the data are acquired on Device A. For $T > 50$ K, a strong temperature dependence suggests phonon scattering dominated transport. The mobility saturates at $T < 50$ K, limited by long-range Coulomb scattering.

The intrinsic carrier mobility $\mu = G_{\square}/(ne)$ can be calculated using the measured $G_{\square}$ and n values. Absent carrier density measurements, a separate, and often used metric is the two- or four-point field-effect mobility $\mu_{FE} = (L/W) \times (dG/dV_G) \times {C_G}^{-1}$, where G is the two- or four-point conductance, and V_G and C_G are top/back gate bias and capacitance**.** To assess the accuracy of this metric, we compare the two and four-point μ_{FE} with the intrinsic μ value. Figure 4.7 shows μ vs T at different n values, along with μ_{FE} vs. T extracted from G_{4pt} vs. V_{TG} data. At room temperature, the intrinsic mobility at the highest electron density 9×10^{12} cm^{-2} is 100 cm^2/(V·s), and increases rapidly with decreasing temperature, reaching 2,000 cm^2/(V·s) at 1.5 K, which is a record-high electron mobility probed in monolayer WS_2.

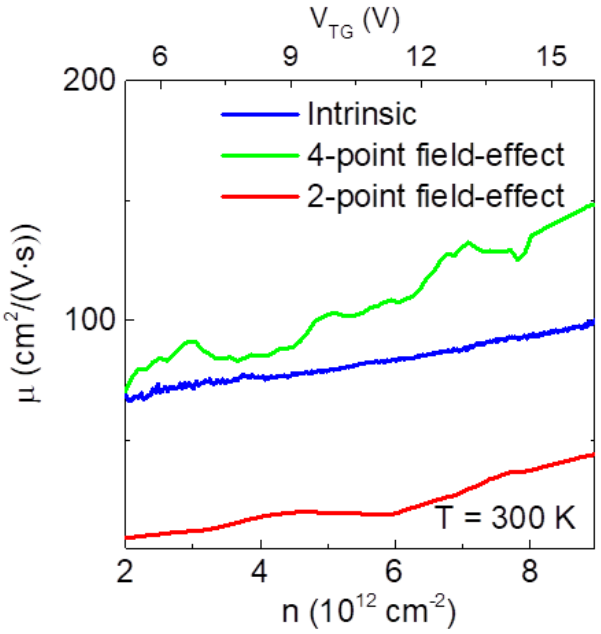

Figure 4.8: μ vs. n at room temperature. The comparison includes the intrinsic mobility, as well as the two- and four-point field-effect mobilities. The bottom and top axes are the Hall density and top gate bias, respectively. The four-point field-effect mobility overestimates the intrinsic mobility, while two-point field-effect mobility underestimates the intrinsic mobility by approximately 50%.

In Fig. 4.8 we compare the intrinsic, two-point, and four-point field-effect mobilities at room temperature. The four-point field-effect values are consistently larger compared to the intrinsic mobility, similar to observations reported in MoS_2 FETs.[9] To explain this observation let us assume the dielectric-TMD interface has a density (D_{it}) of traps per unit area×energy at the Fermi energy. A change in gate bias (dV_G) will induce a change in both the density of the trapped charges dn_{it} and the mobile electron density dn, $C_G dV_G = e(dn_{it} + dn)$. In thermodynamic equilibrium, $dn_{it}/dn = D_{it}/DOS$, where DOS is the density of states of the 2D system at the Fermi energy. The four-point field effect mobility then is

$$\mu_{FE} = \frac{1}{C_G} \cdot \frac{dG_{\square}}{dn} \cdot \frac{dn}{dV_G} = \frac{\mu + n(d\mu/dn)}{1 + D_{it}/DOS}. \quad (4.5)$$

For a TMD layer with two-fold valley degeneracy $DOS = 2m^*/(\pi\hbar^2)$, where m^* is the effective mass, and $\hbar$ the reduced Planck constant. Using $m^* = 0.5m_e$, a typical value for TMDs, the corresponding $DOS = 4 \times 10^{14}$ cm^{-2} eV^{-1}. The intrinsic defect density in exfoliated TMDs determined from scanning probe microscopy is ~10^{12} cm^{-2},[43,44] and even for a gate-stack of moderate quality the corresponding D_{it} should be at least one order of magnitude lower compared to DOS. Therefore, the term D_{it}/DOS in Eq. (4.5) can be neglected. This approximation is also supported by the very good agreement between the geometric gate capacitances, and their values determined by Hall measurements in our experiment. Equation (4.5) then is $\mu_{FE} - \mu = n(d\mu/dn)$. If the μ value increases with n, which is expected if screening plays a role in the scattering mechanism, the four-point field-effect mobility will overestimate the intrinsic mobility. We note that scattering mechanisms such as surface roughness or carrier confinement which normally lead to a reduction in mobility at high carrier densities in inversion layers realized in bulk semiconductors either do not apply, or do not have the same density dependence in 2D

materials. Indeed, the surface roughness is not expected to reduce the mobility at high densities in 2D materials because the electron wave-function does not change appreciably with gate bias. Moreover, the confinement in the 2D plane does not lead to multiple subbands as one might encounter in the triangular well of a metal-oxide-semiconductor FET.

It is noteworthy that the two-point field-effect mobility significantly underestimates the mobility by ~50%, which can be attributed to the voltage drop on the source/drain, and the gate-dependent contact resistances.

Chapter 5: Theoretical Modeling

5.1 Scattering Mechanisms in 2D Electron System

In this section we review some scattering mechanisms relevant in 2D electron systems and the electron mobility modeling associated with each scattering mechanism. Three important scattering mechanisms will be discussed in the following sections – optical phonon scattering, acoustic phonon scattering, and ionized impurity scattering.

5.1.1 Optical Phonon Scattering

There are two types of optical phonons considered in this section – polar optical phonon and homopolar optical phonon. In the polar optical phonon mode, all the atom motions are in-plane. For WS_2 atom, the two sulfur atoms in a WS_2 molecule move in the same direction, while the tungsten atom moves in the opposite direction, as illustrated in Fig. 5.1 (a).

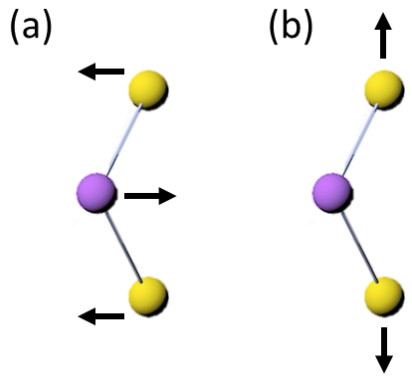

Figure 5.1: Optical phonon modes. (a) polar optical phonon mode, (b) homopolar optical phonon mode.

The expression of polar optical phonon associated mobility can be written as[45,46]

$$\mu_{po} = \frac{4\pi\varepsilon_0\varepsilon_p\hbar^2}{e\omega m^{*2}Z_0}\left(e^{\frac{\hbar\omega}{k_BT}} - 1\right), \tag{5.1}$$

where e is electron charge, $\hbar\omega$ is the polar optic phonon energy, m^* is the electron effective mass, Z_0 is the layer thickness, $\frac{1}{\varepsilon_p} = \frac{1}{\varepsilon_\infty} - \frac{1}{\varepsilon_s}$, ε_∞ and ε_s are the high and low frequency dielectric constants. From Eq. (5.1), at high temperatures polar optical phonon can be the limiting term in electron mobility.

In the homopolar phonon mode, the two sulfur atoms move out-of-plane, in opposite directions, and the tungsten atom is stationary, as illustrated in Fig. 5.1 (b). Because the motions of the sulfur atoms are mirrored image to each other, and the center of mass is unaffected by this motion, no first-order dipole is produced, therefore this mode is "homopolar". The mobility associated with the homopolar phonon mode has a stronger dependence on temperature compared to the polar mode.[47] However, it is found that in top-gated 2D FETs, due to the presence of the gate dielectrics and metal gates, the vertical motions can be restricted, and the homopolar mode can be quenched.[48,49] Therefore, homopolar optical phonon scattering is not expected to be one of the dominant scattering mechanisms in our devices.

5.1.2 Acoustic Phonon Scattering

In Ref. [48], the mobility associated with the acoustic phonon scattering is deduced based on Boltzmann transport theory. Assuming high temperature, quasielastic and isotropic scattering, the acoustic phonon limited mobility can be written as

$$\mu_{ac} = \frac{e\hbar^3 \rho {c_\lambda}^2}{m^{*2}\Xi^2 k_B T} \tag{5.2}$$

where ρ is the atomic mass density per area, c_λ is the sound velocity, and Ξ is the acoustic deformation potential. If writing the temperature dependence of μ in the form of $\mu \propto T^{-\gamma}$, the temperature dependence coefficient γ deduced in this acoustic phonon

scattering model yields $\gamma = 1$. We shall note that Eq. (5.2) is a result considering only deformation potential contribution from intravalley zone center acoustic phonon scattering.

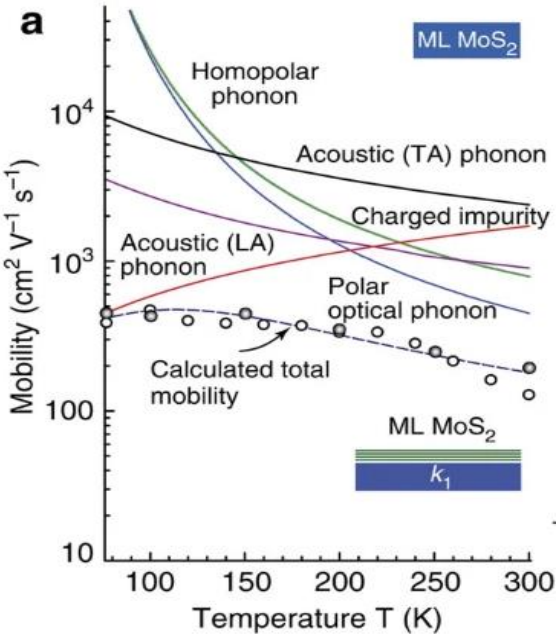

Figure 5.2: Temperature dependence of electron mobility calculated for different scattering mechanisms for few-layer (multilayer) MoS_2 FETs on Al_2O_3. Optical phonons (green and blue lines) dominate at high temperature, while acoustic phonons (brown and purple lines) become important at intermediate temperature. Figure adapted form Ref. [50].

Acoustic phonon scattering is usually important at intermediate temperature. As shown in Fig. 5.2, where the temperature dependence of mobilities associated with various scattering mechanisms are calculated for a few-layer MoS_2 FET without top gate.[50] At high temperature, optical phonon will be the limiting factor for electron mobility as discussed in Section 5.1.1. At around 200 K, when largest, the contribution from the acoustic phonon could be comparable to optical phonon. At lower temperature, all the phonon modes will

be frozen out, and ionized impurity scattering will take over, which we will discuss in the next session.

5.1.3 Ionized Impurity Scattering

In monolayer TMD electron systems, ionized impurity scattering can be largely affected by the dielectric environment. In Fig. 5.3, the Coulomb potentials calculated for a point charge located at the center of a monolayer MoS_2 encapsulated in different dielectric environments are shown.[51] The Coulomb potential in the dielectric with lower dielectric constant ε_e extends further while in high-ε_e environment decays faster. This can be explained by larger energy barrier for confining electrons provided by high-ε_e dielectrics. The other effect the dielectric environment has on electron transport is that the electrons in the TMD thin layer can also remotely excite the polar optical phonon in the dielectrics. This effect strengthens as the thickness of the TMD layer is decreased.

Figure 5.3 is calculated without considering the screening effect.[51] Taking the free-carrier screening into account, in Ref. [51], the Coulomb momentum relaxation rate is calculated from the Fermi's golden rule, at the zero-temperature limit, with the impurity density set to be $N_I \sim 10^{12}\ cm^{-2}$. This calculation combines free-carrier screening with the effects of dielectric environment on the Coulomb interactions. In Figure 5.4 (a), the Coulomb momentum relaxation rate as a function of ε_e and the electron density is shown. The relaxation rate decreases with increased electron density and dielectric constant. The electron density dependence of the relaxation rate is a manifestation of the screening effect.

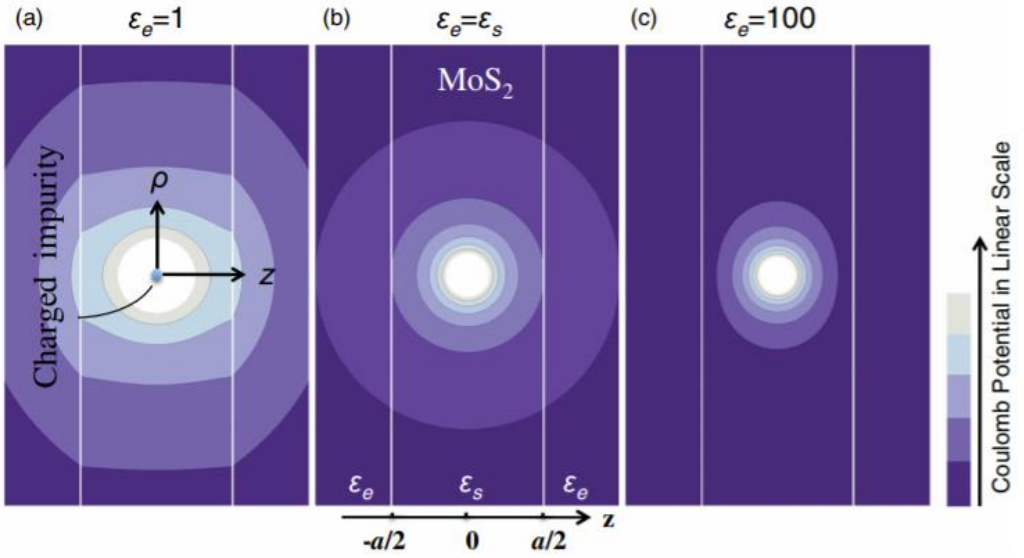

Figure 5.3: Coulomb potentials of a point charge at the center of a MoS_2 monolayer encapsulated by two dielectric layers, for (a) $\varepsilon_e = 1$, (b) $\varepsilon_e = 7.6\ (= \varepsilon_s$, dielectric constant of MoS_2), and (c) $\varepsilon_e = 100$. Figure adapted form Ref. [51].

With the temperature effect on the polarizability of the electron gas taken into consideration, which is caused by the spatial redistribution of the electron gas induced by the Coulomb potential, the temperature dependence of the mobility associated with the impurity scattering is shown in Fig. 5.4 (b). The impurity density used in this calculation is $10^{13}\ cm^{-2}$. It can be seen from Fig. 5.4 (b) that the mobility is significantly limited by ionized impurity scattering at low electron density and low ε_e. At high electron densities relevant to the electron systems discussed in this thesis (~$10^{13}\ cm^{-2}$), the temperature dependence of the impurity limited mobility is very weak at $T < 50\ K$. It is also worth noting that, in our devices, the mobility measured at low temperature, when the impurity scattering dominates due to freeze-out of the phonons, is about an order of magnitude larger than the theoretical calculations in Fig. 5.4 (b). This is a manifestation of the low ionized impurity density in our channel material.

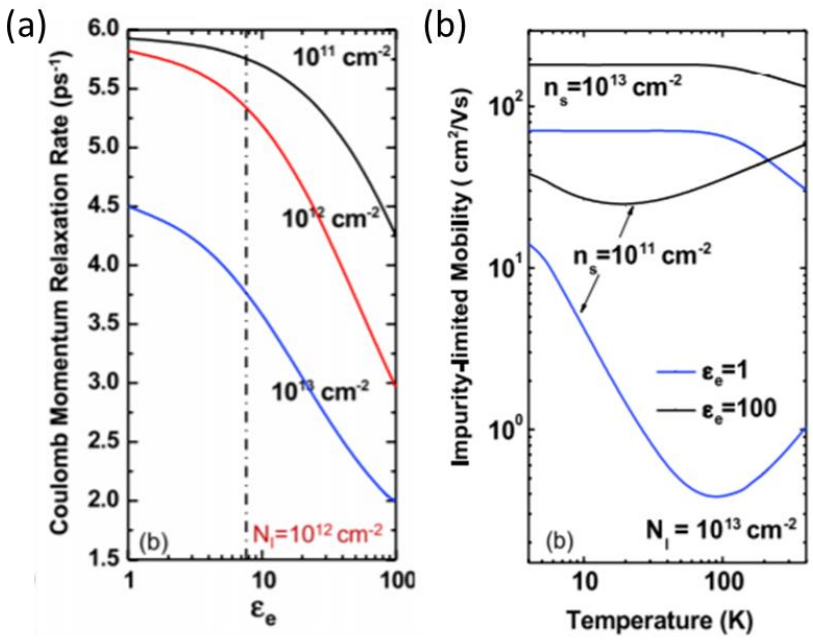

Figure 5.4: (a) Effect of dielectric mismatch and electron density on Coulomb momentum relaxation time at zero temperature limit and (b) impurity limited mobility as a function of temperature at different electron densities. Panel (a) is calculated with impurity density of $10^{12}\,cm^{-2}$, panel (b) $10^{13}\,cm^{-2}$. n_s is the electron density in the TMD layer. Figure adapted form Ref. [51].

5.2 First Principles Phonon Scattering Calculations

This section will serve as an introduction of the first principles method used to calculate the temperature dependence of the mobility, which will provide comparison of the experimental results to the intrinsic limit of transport in our WS_2 monolayer. The details of this method can be found in Ref. [52].

5.2.1 Boltzmann Transport Equation

For a 2D system lying in the x-y plane with an electric field $\boldsymbol{E}$ applied in the same plane, in the $-\boldsymbol{u_E}$ direction, the expression of conductivity is

$$\sigma = \sum_{\alpha} \frac{2e}{|\boldsymbol{E}|} \int_{k\in\alpha} \frac{d\boldsymbol{k}}{(2\pi)^2} f(\boldsymbol{k}) \boldsymbol{v}(\boldsymbol{k}) \cdot \boldsymbol{u}_E, \tag{5.3}$$

where the factor of 2 accounts for the spin degeneracy, α is an index of valleys in the Brillouin zone, $f(\boldsymbol{k})$ is the steady-state distribution function, and $\boldsymbol{v}(\boldsymbol{k})$ is the band velocity of the electronic state. Assuming spatial uniformity and time-independence (steady state), Boltzmann transport equation (BTE) can be written as

$$-\frac{e\boldsymbol{E}}{\hbar}\cdot\frac{\partial f}{\partial \boldsymbol{k}}=\left(\frac{\partial f}{\partial t}\right)_{scatt}(\boldsymbol{k}). \tag{5.4}$$

Eq. (5.4) states that the change of the occupation distribution driven by the electric field equals to the time derivation of the distribution function due to scattering. Using Fermi's golden rule, the right-hand side of Eq. (5.4) can be written as

$$\left(\frac{\partial f}{\partial t}\right)_{scatt}(\boldsymbol{k})=\sum_{\boldsymbol{k}'}P_{\boldsymbol{k}'\boldsymbol{k}}f(\boldsymbol{k}')\big(1-f(\boldsymbol{k})\big)-P_{\boldsymbol{k}\boldsymbol{k}'}f(\boldsymbol{k})\big(1-f(\boldsymbol{k}')\big), \tag{5.5}$$

where $P_{\boldsymbol{k}\boldsymbol{k}'}$ is the scattering probability from state $\boldsymbol{k}$ to $\boldsymbol{k}'$.

A perturbation at first order in electric field is adopted and the occupation function is written as

$$f(\boldsymbol{k})=f^0(\boldsymbol{k})+f^1(\boldsymbol{k}). \tag{5.6}$$

Here, $f^0(\boldsymbol{k})$ is the Fermi-Dirac function, and $f^1(\boldsymbol{k})$ is the first-order perturbation in the electric field, and

$$f^1(\boldsymbol{k})=e|\boldsymbol{E}|\boldsymbol{u}_{\boldsymbol{E}}\cdot\boldsymbol{F}(\boldsymbol{k})\frac{\partial f^0(\boldsymbol{k})}{\partial\varepsilon}, \tag{5.7}$$

where ε is the electron state energy, $\boldsymbol{F}(\boldsymbol{k})$ is a vectorial quantity with units of length, whose direction is assumed to be along the band velocity, such that

$$\boldsymbol{F}(\boldsymbol{k})=\boldsymbol{v}(\boldsymbol{k})\tau(\boldsymbol{k}), \tag{5.8}$$

$\tau(\boldsymbol{k})$ is named as scattering time. Combing Eq. (5.6)-(5.8), and keeping only first-order terms in the electric field, with the detailed balance condition $P_{\boldsymbol{k'k}} f^0(\boldsymbol{k'})\big(1 - f^0(\boldsymbol{k})\big) = P_{\boldsymbol{kk'}} f^0(\boldsymbol{k})\big(1 - f^0(\boldsymbol{k'})\big)$ and the relation $\frac{\partial f^0(\boldsymbol{k})}{\partial \varepsilon} = \frac{f^0(\boldsymbol{k})(1-f^0(\boldsymbol{k}))}{kT}$, one gets

$$(1 - f^0(\boldsymbol{k}))\boldsymbol{v}(\boldsymbol{k}) \cdot \boldsymbol{u_E} = \sum_{\boldsymbol{k'}} P_{\boldsymbol{kk'}}\big(1 - f^0(\boldsymbol{k'})\big) \times \{\boldsymbol{v}(\boldsymbol{k}) \cdot \boldsymbol{u_E}\tau(\boldsymbol{k}) - \boldsymbol{v}(\boldsymbol{k'}) \cdot \boldsymbol{u_E}\tau(\boldsymbol{k'}), \quad (5.9)$$

which will be referred to as the linearized BTE. Combing Eq. (5.3) and (5.6), the expression of conductivity can be written as

$$\sigma = \sum_\alpha 2e^2 \int_{k\in\alpha} \frac{d\boldsymbol{k}}{(2\pi)^2} (\boldsymbol{v}(\boldsymbol{k}) \cdot \boldsymbol{u}_E)^2 \ \tau(\boldsymbol{k}) \frac{\partial f^0(\boldsymbol{k})}{\partial \varepsilon}. \quad (5.10)$$

This expression will be used to calculate the conductivity and mobility of the simulated electron system. It is worth noting that, to compute the conductivity, very few approximations – linear order in electric field, steady state, and $\boldsymbol{F}(\boldsymbol{k})$ along band velocity – are made, in addition to one more approximation on equilibrium phonon distribution, addressed in the next section. We highlight that this method is beyond relaxation time approximation, which is commonly used in first principles methods.

5.2.2 Electron-Phonon Coupling Matrix

The scattering probability $P_{\boldsymbol{kk'}}$ from Eq. (5.5) includes all the relevant scattering processes in the system. Summing over all phonon modes, $P_{\boldsymbol{kk'}}$ can be written as $P_{\boldsymbol{kk'}} = \sum_\nu P_{\boldsymbol{kk'},\nu}$, where ν is an index for phonon modes, and $P_{\boldsymbol{kk'},\nu}$ is the sum of the emission and absorption associate with the mode ν of the momentum $q = k' - k$, and is

$$P_{\boldsymbol{kk+q},\nu} = \frac{2\pi}{\hbar}\frac{1}{N}\left|g_{\boldsymbol{kk+q},\nu}\right|^2 \{n_{\boldsymbol{q},\nu}\delta\big(\varepsilon_{\boldsymbol{k+q}} - \varepsilon_{\boldsymbol{k}} - \hbar\omega_{\boldsymbol{q},\nu}\big) + (n_{\boldsymbol{q},\nu} + 1)\big(\varepsilon_{\boldsymbol{k+q}} - \varepsilon_{\boldsymbol{k}} + \hbar\omega_{\boldsymbol{q},\nu}\big). \quad (5.11)$$

$g_{\boldsymbol{kk+q},\nu}$ in Eq. (5.11) is the electron-phonon coupling (EPC) matrix element, and $n_{\boldsymbol{q},\nu}$ is the phonon occupation, which is assumed to be the equilibrium Bose-Einstein distribution. The EPC matrix can be computed within the density-functional perturbation theory (DFPT).

5.2.3 Workflow and Discussion

The workflow of the first principles calculations is as the following: (1) band structures are calculated within density-functional theory; (2) EPC matrix elements are computed within DFPT; (3) Using the EPC elements, $P_{\boldsymbol{kk'}}$ is computed and the BTE is solved iteratively. $\tau(\boldsymbol{k})$ can then be computed and integrated to acquire temperature dependent mobility.

We highlight the strengths of this first principles method by discussing two important aspects when evaluating electronic transport in 2D systems – doping effect and intravalley coupling. In this method, doping effect is accounted for via a recent-developed DFPT for gated materials,[53] where the electrostatic gating is modeled. In contrast to some theoretical calculation studies where charging is treated as a rigid shift of the Fermi level and the effect of doping on EPC is neglected, or where screening effects are considered analytically[48] and various approximations are made, this method includes doping explicitly to not only take into account the screening effects on the EPC, but also other effects on scattering, such as the activation of intervalley scattering, etc. Intervalley scattering is also an important factor to consider – which is also rarely included in other transport models in 2D TMD systems. It turns out that intervalley scattering has a significant effect on the temperature dependent mobility simulations, which will be addressed in the next session. Note that in the above discussion, spin-orbit coupling (SOC) is not considered. However,

by including SOC into band structure calculations, we are able to incorporate SOC into the mobility calculation results, as done in the next section.

5.3 CALCULATION SETUPS AND RESULTS

In this section, we will review the μ vs. T data measured in our WS_2 monolayer devices and compared the experimental data with theoretical calculation results. The theoretical calculations are performed in collaboration with Thibault Sohier and Matthieu Verstraete in Université de Liege.

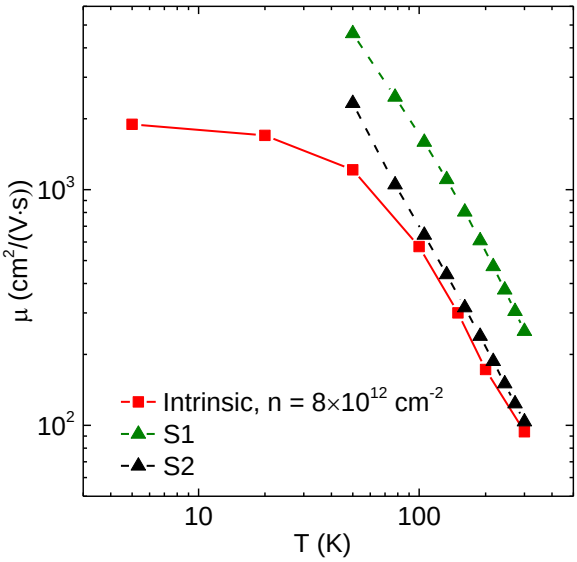

Figure 5.5: Comparison of experimental and theoretical results of μ vs. T. Square symbols represent experimental results of intrinsic mobility at electron density 8×10^{12} cm^{-2}, triangular symbols represent theoretical calculation results, at the same carrier density.

In Fig. 5.5, temperature dependence of the intrinsic mobility at electron density 8×10^{12} cm^{-2} (data taken from Fig. 4.7) is plotted. At high temperature (T > 50 K), The

temperature dependence of the electron mobility follows approximately a power law $\mu \propto T^{-\gamma}$, and a functional fit of the data yields γ = 1.46. As discussed in Section 5.1.2, intravalley scattering from zone center acoustic phonons in a deformation potential model leads to γ = 1.[48] Thus, γ > 1 suggests a more complex combination of both intra- and intervalley contributions from acoustic and optical phonons, which we confirm through first principles calculations. At low temperature, the mobility saturates at ~2,000 $cm^2/(V \cdot s)$, which can be explained by ionized impurity scattering.[51]

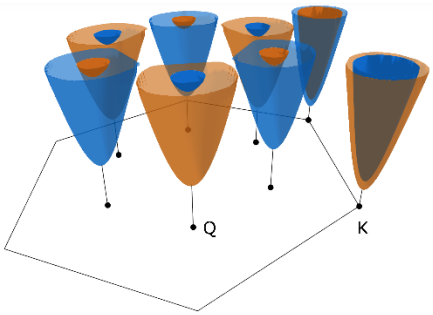

Figure 5.6: The multivalley, spin-textured band structure of WS_2 as computed in first principles. Only the inequivalent K and Q valleys in one Brillouin zone are presented. Orange and blue colors represent opposite spin-textures.

Figure 5.5 also shows first-principles calculation results of the intrinsic, phonon-limited mobility of WS_2. The electron-phonon interactions are computed within DFPT,[54,55] and Optimized Norm-Conserving Vanderbilt pseudopotentials[56] from the PseudoDojo library.[57] The full momentum- and energy-dependent Boltzmann transport equation is solved iteratively as discussed in Section 5.2. An electrostatic doping of 8×10^{12} cm^{-2}, same electron density as the experimental result (red) shown in Fig. 5.5, is explicitly included[53] to account for free-carrier screening and the potential enhancement of electron-phonon interactions induced by multivalley occupation in TMDs[58]. Spin-orbit interaction is

included in all simulations as previously mentioned in Section 5.2.3. As depicted in Fig. 5.6, the conduction band is composed of K and Q valleys, each split by spin-orbit interactions.

Transport simulations are highly sensitive to the details of this complex band structure, and in particular to the relative positions of the valleys and the Fermi level, which are in turn sensitive to the computational details. In an effort to capture this, Fig. 5.5 reports mobility for two slightly different structures: S1 and S2. The lattice parameters in S1 and S2 are identical ($a_1 = a_2 = 3.187$ Å) while the layer thickness in S2 is only 0.4% larger ($t_1 = 3.14$ Å, $t_2 = 3.15$ Å) which is within density-functional theory structural precision. Both structures are realistic, a similar variation in thickness may occur in real devices due to encapsulation or substrate interaction. The K - Q valley splittings are 90 meV for S1 and 54 meV for S2, respectively. Small variations are also present in the Fermi velocity (~10% smaller for S2), and the spin-orbit splitting at the K point (30 meV for S1 vs. 33 meV for S2). Many-body, polaronic, and other encapsulation effects could have comparable impact. The mobility values calculated using set-up S1 are higher compared to set-up S2, mainly because of the higher Q valley energy for the former structure, which suppresses K-Q intervalley scattering[52] and allows free carriers to screen the coupling to homopolar optical phonons.[58] The agreement between experiment and simulations is good in magnitude and in the temperature dependence above 50 K. We conclude that the experimental results are very close to the intrinsic, phonon-limited regime, and that the electron-phonon physics is fully captured by the simulations.

Chapter 6: Summary

In summary, a comprehensive study of the monolayer WS_2 field-effect transistors is presented in this thesis. We introduce the fabrication of such devices from scratch – the exfoliation process that produces the atomically thin WS_2 as the base material is described in Chapter 2, followed by the fabrication process flow to construct the 2D heterostructure in Chapter 3.

In Chapter 4, we report the electron transport measured in our WS_2 field-effect transistors and demonstrate the electron density and intrinsic mobility extraction methods through magneto-transport measurements. A high electron mobility of 2,000 $cm^2/(V \cdot s)$ was measured at 1.5 K. We discussed the Ohmic nature of our WS_2-to-metal contacts, which is robust at cryogenic temperatures down to 1.5 K. In addition, we compared three types of methods to evaluate the electron mobility, and we conclude that four-point and two-point field-effect mobilities overestimate and underestimate carrier mobilities in 2D TMD systems, respectively.

A review of important scattering mechanisms in 2D electron systems is presented in Chapter 5, as well as first-principles calculation results of the phonon-limited mobility of WS_2. Good agreement with theoretical predictions confirms the quality of the devices and indicates transport properties close the intrinsic limit.

References

1. Wilson, J. A. & Yoffe, A. D. The transition metal dichalcogenides discussion and interpretation of the observed optical, electrical and structural properties. *Advances in Physics* **18**, 193–335 (1969).
2. Wang, Q. H., Kalantar-Zadeh, K., Kis, A., Coleman, J. N. & Strano, M. S. Electronics and optoelectronics of two-dimensional transition metal dichalcogenides. *Nature Nanotechnology* **7**, 699–712 (2012).
3. Chhowalla, M. *et al.* The chemistry of two-dimensional layered transition metal dichalcogenide nanosheets. *Nature Chemistry* **5**, 263–275 (2013).
4. Zhao, W. *et al.* Evolution of Electronic Structure in Atomically Thin Sheets of WS_2 and WSe_2. *ACS Nano* **7**, 791–797 (2013).
5. Mak, K. F., Lee, C., Hone, J., Shan, J. & Heinz, T. F. Atomically Thin MoS_2: A New Direct-Gap Semiconductor. *Physical Review Letters* **105**, 136805 (2010).
6. Splendiani, A. *et al.* Emerging Photoluminescence in Monolayer MoS_2. *Nano Letters* **10**, 1271–1275 (2010).
7. Radisavljevic, B., Radenovic, A., Brivio, J., Giacometti, V. & Kis, A. Single-layer MoS_2 transistors. *Nature Nanotechnology* **6**, 147–150 (2011).
8. Lembke, D. & Kis, A. Breakdown of High-Performance Monolayer MoS_2 Transistors. *ACS Nano* **6**, 10070–10075 (2012).
9. Baugher, B. W. H., Churchill, H. O. H., Yang, Y. & Jarillo-Herrero, P. Intrinsic Electronic Transport Properties of High-Quality Monolayer and Bilayer MoS_2. *Nano Letters* **13**, 4212–4216 (2013).
10. Movva, H. C. P. *et al.* High-Mobility Holes in Dual-Gated WSe_2 Field-Effect Transistors. *ACS Nano* **9**, 10402–10410 (2015).

11. Gong, C. *et al.* Electronic and Optoelectronic Applications Based on 2D Novel Anisotropic Transition Metal Dichalcogenides. *Advanced Science* **4**, 1700231 (2017).
12. Yin, Z. *et al.* Single-Layer MoS $_2$ Phototransistors. *ACS Nano* **6**, 74–80 (2012).
13. Lopez-Sanchez, O., Lembke, D., Kayci, M., Radenovic, A. & Kis, A. Ultrasensitive photodetectors based on monolayer MoS2. *Nature Nanotechnology* **8**, 497–501 (2013).
14. Cao, T. *et al.* Valley-selective circular dichroism of monolayer molybdenum disulphide. *Nature Communications* **3**, 887 (2012).
15. Mak, K. F., McGill, K. L., Park, J. & McEuen, P. L. The valley Hall effect in MoS2 transistors. *Science* **344**, 1489–1492 (2014).
16. Safeer, C. K. *et al.* Room-Temperature Spin Hall Effect in Graphene/MoS_2 van der Waals Heterostructures. *Nano Letters* **19**, 1074–1082 (2019).
17. Jin, Z., Li, X., Mullen, J. T. & Kim, K. W. Intrinsic transport properties of electrons and holes in monolayer transition-metal dichalcogenides. *Physical Review B* **90**, 045422 (2014).
18. Chernikov, A. *et al.* Exciton Binding Energy and Nonhydrogenic Rydberg Series in Monolayer WS_2. *Physical Review Letters* **113**, 076802 (2014).
19. Hsu, W.-T. *et al.* Dielectric impact on exciton binding energy and quasiparticle bandgap in monolayer WS_2 and WSe_2. *2D Materials* **6**, 025028 (2019).
20. Liu, L., Kumar, S. B., Ouyang, Y. & Guo, J. Performance Limits of Monolayer Transition Metal Dichalcogenide Transistors. *IEEE Transactions on Electron Devices* **58**, 3042–3047 (2011).

21. Kormányos, A., Zólyomi, V., Drummond, N. D. & Burkard, G. Spin-Orbit Coupling, Quantum Dots, and Qubits in Monolayer Transition Metal Dichalcogenides. *Physical Review X* **4**, 011034 (2014).

22. Braga, D., Gutiérrez Lezama, I., Berger, H. & Morpurgo, A. F. Quantitative Determination of the Band Gap of WS_2 with Ambipolar Ionic Liquid-Gated Transistors. *Nano Letters* **12**, 5218–5223 (2012).

23. Ovchinnikov, D., Allain, A., Huang, Y.-S., Dumcenco, D. & Kis, A. Electrical Transport Properties of Single-Layer WS_2. *ACS Nano* **8**, 8174–8181 (2014).

24. Liu, X. *et al.* High Performance Field-Effect Transistor Based on Multilayer Tungsten Disulfide. *ACS Nano* **8**, 10396–10402 (2014).

25. Iqbal, M. W. *et al.* High-mobility and air-stable single-layer WS_2 field-effect transistors sandwiched between chemical vapor deposition-grown hexagonal BN films. *Scientific Reports* **5**, 10699 (2015).

26. Cui, Y. *et al.* High-Performance Monolayer WS_2 Field-Effect Transistors on High-κ Dielectrics. *Advanced Materials* **27**, 5230–5234 (2015).

27. Zeng, H. *et al.* Optical signature of symmetry variations and spin-valley coupling in atomically thin tungsten dichalcogenides. *Scientific Reports* **3**, 1608 (2013).

28. Gutiérrez, H. R. *et al.* Extraordinary Room-Temperature Photoluminescence in Triangular WS_2 Monolayers. *Nano Letters* **13**, 3447–3454 (2013).

29. Jo, S., Ubrig, N., Berger, H., Kuzmenko, A. B. & Morpurgo, A. F. Mono- and Bilayer WS_2 Light-Emitting Transistors. *Nano Letters* **14**, 2019–2025 (2014).

30. Novoselov, K. S. *et al.* Electric Field Effect in Atomically Thin Carbon Films. *Science* **306**, 666–669 (2004).

31. Häkkinen, H. The gold–sulfur interface at the nanoscale. *Nature Chemistry* **4**, 443–455 (2012).

32. Grönbeck, H., Curioni, A. & Andreoni, W. Thiols and Disulfides on the Au(111) Surface: The Headgroup−Gold Interaction. *Journal of the American Chemical Society* **122**, 3839–3842 (2000).

33. Desai, S. B. *et al.* Gold-Mediated Exfoliation of Ultralarge Optoelectronically-Perfect Monolayers. *Advanced Materials* **28**, 4053–4058 (2016).

34. Velický, M. *et al.* Mechanism of Gold-Assisted Exfoliation of Centimeter-Sized Transition-Metal Dichalcogenide Monolayers. *ACS Nano* **12**, 10463–10472 (2018).

35. Reina, A. *et al.* Transferring and Identification of Single- and Few-Layer Graphene on Arbitrary Substrates. *The Journal of Physical Chemistry C* **112**, 17741–17744 (2008).

36. Frisenda, R. *et al.* Recent progress in the assembly of nanodevices and van der Waals heterostructures by deterministic placement of 2D materials. *Chemical Society Reviews* **47**, 53–68 (2018).

37. Hall, E. H. On a New Action of the Magnet on Electric Currents. *American Journal of Mathematics* **2**, 287–292 (1879).

38. Klitzing, K. v., Dorda, G. & Pepper, M. New Method for High-Accuracy Determination of the Fine-Structure Constant Based on Quantized Hall Resistance. *Physical Review Letters* **45**, 494 (1980).

39. Laughlin, R. B. Quantized Hall conductivity in two dimensions. *Physical Review B* **23**, 5632(R) (1981).

40. Haldane, F. D. M. Model for a Quantum Hall Effect without Landau Levels: Condensed-Matter Realization of the “Parity Anomaly.” *Physical Review Letters* **61**, 2015 (1988).

41. Appenzeller, J., Radosavljević, M., Knoch, J. & Avouris, Ph. Tunneling Versus Thermionic Emission in One-Dimensional Semiconductors. *Physical Review Letters* **92**, 048301 (2004).

42. Das, S., Chen, H.-Y., Penumatcha, A. V. & Appenzeller, J. High Performance Multilayer MoS_2 Transistors with Scandium Contacts. *Nano Letters* **13**, 100–105 (2013).

43. Lu, C.-P., Li, G., Mao, J., Wang, L.-M. & Andrei, E. Y. Bandgap, Mid-Gap States, and Gating Effects in MoS_2. *Nano Letters* **14**, 4628–4633 (2014).

44. Addou, R., Colombo, L. & Wallace, R. M. Surface Defects on Natural MoS_2. *ACS Applied Materials & Interfaces* **7**, 11921–11929 (2015).

45. Ridley, B. K. The electron-phonon interaction in quasi-two-dimensional semiconductor quantum-well structures. *Journal of Physics C: Solid State Physics* **15**, (1982).

46. Lisesivdin, S. B. *et al.* Scattering analysis of 2DEG carrier extracted by QMSA in undoped $Al_{0.25}Ga_{0.75}N$/GaN heterostructures. *Semiconductor Science and Technology* **22**, (2007).

47. Fivaz, R. & Mooser, E. Mobility of Charge Carriers in Semiconducting Layer Structures. *Physical Review* **163**, (1967).

48. Kaasbjerg, K., Thygesen, K. S. & Jacobsen, K. W. Phonon-limited mobility in n-type single-layer MoS_2 from first principles. *Physical Review B* **85**, 115317 (2012).

49. Radisavljevic, B. & Kis, A. Mobility engineering and a metal–insulator transition in monolayer MoS_2. *Nature Materials* **12**, 815–820 (2013).

50. Kim, S. *et al.* High-mobility and low-power thin-film transistors based on multilayer MoS_2 crystals. *Nature Communications* **3**, 1011 (2012).

51. Ma, N. & Jena, D. Charge Scattering and Mobility in Atomically Thin Semiconductors. *Physical Review X* **4**, 011043 (2014).

52. Sohier, T., Campi, D., Marzari, N. & Gibertini, M. Mobility of two-dimensional materials from first principles in an accurate and automated framework. *Physical Review Materials* **2**, 114010 (2018).

53. Sohier, T., Calandra, M. & Mauri, F. Density functional perturbation theory for gated two-dimensional heterostructures: Theoretical developments and application to flexural phonons in graphene. *Physical Review B* **96**, 075448 (2017).

54. Giannozzi, P. *et al.* QUANTUM ESPRESSO: a modular and open-source software project for quantum simulations of materials. *Journal of Physics: Condensed Matter* **21**, 395502 (2009).

55. Giannozzi, P. *et al.* Advanced capabilities for materials modelling with Quantum ESPRESSO. *Journal of Physics: Condensed Matter* **29**, 465901 (2017).

56. Hamann, D. R. Optimized norm-conserving Vanderbilt pseudopotentials. *Physical Review B* **88**, 085117 (2013).

57. van Setten, M. J. *et al.* The PseudoDojo: Training and grading a 85 element optimized norm-conserving pseudopotential table. *Computer Physics Communications* **226**, 39–54 (2018).

58. Sohier, T. *et al.* Enhanced Electron-Phonon Interaction in Multivalley Materials. *Physical Review X* **9**, 031019 (2019).